J Adv Ceram 2025, **15**: 9221233

https://doi.org/10.26599/JAC.2025.9221233

Research Article

CuO-decorated bismuth subcarbonate p-n heterostructured micro-flowers for high-selectivity VOC gas sensor arrays and cooked rice quality assessment

Zichen Zheng[1,2,3], Kewei Liu[1,2,4], Yiwen Zhou[1,2], Kaichun Xu[1,2,5],
Changlong Wang[1], Marc Debliquy[4], Carla Bittencourt[3], Chao Zhang[1,2,*]

[1] *College of Mechanical Engineering, Yangzhou University, Yangzhou 225127, China*
[2] *Jiangsu Key Laboratory of Surface Strengthening and Functional Manufacturing, Yangzhou University, Yangzhou 225127, China*
[3] *Chimie des Interactions Plasma-Surface, Research Institute for Materials Science and Engineering, University of Mons, Mons 7000, Belgium*
[4] *Service de Science des Matériaux, Research Institute for Materials Science and Engineering, Faculté Polytechnique, University of Mons, Mons 7000, Belgium*
[5] *ICB UMR 6303, CNRS, Univ. Bourgogne Franche-Comté, UTBM, Belfort 90010, France*

* Corresponding author
Email: zhangc@yzu.edu.cn

Received: October 21, 2025; Revised: December 10, 2025; Accepted: December 19, 2025

Abstract: A gas sensor system with high sensitivity and excellent selectivity is essential for accurately evaluating the quality of cooked rice and optimizing agricultural storage conditions in real time. Detecting large molecular volatile organic compounds (VOCs) emitted from cooked rice presents several challenges, including low volatility, interference from complex sample matrices, and limited selectivity. In this study, we propose using $CuO/Bi_2O_2CO_3$ (Cu-BC) p-n heterostructure micro-flowers as a substrate to create a four-channel gas sensor array that converts voltage to resistance. The individual Cux-BC sensors (x = 10, 20, 30, and 40) exhibit a strong response to nonanal, benzaldehyde, and 1-octen-3-ol at room temperature (25 ± 2°C), with detection specificity confirmed through principal component analysis (PCA). This integrated gas sensor array effectively identifies and distinguishes the quality of cooked rice, including both freshly prepared rice and rice stored for one to six weeks. The sensing mechanism relies on increased oxygen vacancies and improved electron mobility. Additionally, we explore the adsorption and diffusion mechanisms of the target gas molecules and oxygen on the surface of the materials using molecular dynamics (MD) simulations. Overall, the gas sensing array demonstrates significant potential in accurately assessing the quality of agricultural products at different storage stages.

Keywords: $Bi_2O_2CO_3$, sensor array, selectivity, heterostructure, cooked rice

1. Introduction

Aroma is among the main quality attributes in foods and beverages, often serving as one of the first characteristics consumers evaluate before tasting the product [1-5]. This sensory aspect is significantly influenced by the presence of volatile organic compounds (VOCs), particularly aldehydes and alcoholic compounds, which are the predominant VOCs released from various types of cooked rice. Consequently, research has concentrated on identifying and analyzing these specific VOCs [6-9]. Among these VOCs, nonanal, benzaldehyde, and 1-octen-3-ol have been frequently reported as abundant odor-active components in cooked rice, mainly originating from lipid oxidation and contributing grassy or fatty, almond-like and mushroom-like notes, respectively [10, 11]. Their concentrations change markedly during storage and show strong correlations with sensory quality, so they are often used as indicator volatiles for evaluating cooked rice aroma and freshness [12, 13]. Therefore, in this work we select nonanal, benzaldehyde, and 1-octen-3-ol as representative target analytes for cooked rice quality monitoring. Traditional methods for their analysis typically involve techniques such as headspace solid phase microextraction (HS-SPME), gas chromatography-mass spectrometry (GC-MS) [7]. However, these techniques have notable limitations, including high amounts sample requirements, complex procedures, and significant costs. Therefore, there is an urgent need for the development of a simple and rapid detection platform.

Ternary metal oxide semiconductor (TMOS) active layers are a fundamental component in chemiresistive sensors and are extensively used for detecting various gases. Their widespread application is attributed to several advantages, including straightforward preparation methods, cost-effectiveness, and operational convenience for users [14-17]. These sensors have applications in non-invasive disease detection

[18], agricultural product testing [19], and wearable devices [20]. Among them, bismuth subcarbonate ($Bi_2O_2CO_3$) is a notable n-type semiconductor characterized by its Aurivillius/Sillén-related structure, formed by alternating layers of $Bi_2O_2^{2+}$ and CO_3^{2-} [21]. This material has been systematically used in energy storage [22], photocatalysis [23], cancer treatment [24], and gas sensing [25] due to its unique physical and chemical properties. However, sensors that rely exclusively on bismuth subcarbonate $Bi_2O_2CO_3$ (BC) often face challenges in achieving high sensitivity, robust stability, and selective detection simultaneously. To address these limitations, we can use the surface depletion mechanism. Specifically, creating an additional electron depletion layer formed at the interface of heterostructured TMOS cores can significantly enhance the gas sensing response compared to a single TMOS [26, 27]. In detail, as a p type semiconductor contacts an n type semiconductor, charge transfer and Fermi level alignment generate a p-n heterojunction with a built-in electric field and an expanded depletion region at the interface. Gas adsorption then strongly modulates the depletion layer width and the interfacial potential barrier, which greatly amplifies the resistance change compared with single phase metal oxide semiconductors (MOS) [28, 29]. In this context, we aimed to enhance the VOCs sensing capabilities by forming CuO/$Bi_2O_2CO_3$ (Cu-BC) heterostructures. CuO was chosen as a p-type metal oxide modifier because it readily forms a p-n heterojunction with n-type BC, increases the concentration of oxygen vacancies (O_V) and catalytically active sites, and reconstructs the BC into semi-hollow micro-flower architectures with a higher specific surface area. These structural and electronic features, together with the narrowed band gap and promoted charge transfer, strengthen the interaction between VOC molecules and the sensing layer, leading to enhanced response and reliable room-temperature sensing performance. This was accomplished by adding $CuCl_2$ with a metal basis grade during the synthesis process.

The use of chemical reagents with a metal basis grade optimizes the electrical and chemical properties of Cu-BC, reduces side reactions during synthesis, and enhances the stability of BC-based materials. This approach facilitates a more controlled preparation of materials. Nevertheless, individual gas sensors continue to encounter several practical challenges, including poor selectivity, limited sensitivity, and susceptibility to environmental influences. Consequently, assembling gas sensors into an array is a more effective strategy for practical detection [30-33]. For instance, Jiang et al. proposed a framework for optimizing gas sensor arrays by considering factors such as material composition, morphology, metal doping, and operating temperature. They established a database using 32 MOS sensors, including SnO_2, In_2O_3, and WO_3, which varied in morphology, dopants (such as Pd, Pt, Ce, Ru, and Rb), and operating temperatures ranging from 250° to 370°C. This database recorded the sensor array responses to six gases at low-ppm concentrations. From a total of 10,518,300 possible material-temperature combinations, an optimized sensor array was constructed, demonstrating enhanced selectivity. Notably, the integrated chip successfully identified all target gases and their mixtures after applying a linear discriminant analysis transformation [34]. Similarly, Yang et al. developed a six-sensor micro-electromechanical systems (MEMS) microarray, along with a wireless, battery-free flexible e-nose controlled by a smartphone. Through the application of ensemble models and algorithms (MLP, RF, XGBoost, and LGBM), they achieved high classification accuracy for VOCs and precise predictions of their concentration. This flexible e-nose offers promising applications in monitoring vehicle and indoor air quality [35].

In this study, we used a single Cu-BC gas sensor to detect nonanal, benzaldehyde, and 1-octen-3-ol individually, thereby validating its initial sensing capabilities for

VOCs at room temperature (25 ± 2°C). Such room temperature operation is advantageous for minimizing energy consumption and enabling safe, practical integration into portable devices [36, 37]. Subsequently, three VOC species were identified in cooked rice by GC-MS to evaluate the effectiveness of the detection method. Finally, we established a gas sensing array consisting of a printed circuit board (PCB) equipped with a 4 × 1 array of data acquisition units featuring voltage conversion and a microcontroller unit for data processing. This array was based on the synthesized Cux-BC materials (where x = 10, 20, 30, and 40) and was designed for efficient detection of cooked rice quality. The integration of Cu-BC-based chemiresistive sensors with embedded electronics presents a promising platform for intelligent food quality monitoring.

2. Materials and Methods

2.1 Chemical Reagents

The reagents were used without further purification. Bismuth nitrate pentahydrate ($Bi(NO_3)_3 \cdot 5H_2O$) (99.99% metals basis, CAS: 10035-06-0), copper(II) chloride ($CuCl_2$) (99.99% metals basis, CAS: 7447-39-4), urea (CH_4N_2O) (AR grade, CAS: 57-13-6), trisodium citrate dihydrate ($C_6H_5Na_3O_7 \cdot 2H_2O$) (AR grade, CAS: 6132-04-3), hexadecyl trimethyl ammonium bromide ($C_{19}H_{42}BrN$) (AR grade, CAS: 57-09-0), sodium hydroxide (NaOH) (AR grade, CAS: 1310-73-2), nitric acid (HNO_3) (ACS, 70%, CAS: 7697-37-2), nonanal ($C_9H_{18}O$) (AR grade, CAS: 124-19-6) and benzaldehyde (C_7H_6O) (AR grade, CAS: 100-52-7) were purchased from Aladdin Biochemical Technology Co., Ltd., China while 1-octen-3-ol ($C_8H_{16}O$) (CAS: 3391-86-4) was obtained through Merck Chemical Technology (Shanghai) Co., Ltd.

2.2 Synthesis of CuOx-BC Micro-structures

The synthetic route of heterostructured $CuO/Bi_2O_2CO_3$ micro-flowers is illustrated in Fig. 1. Typically, 1.94 g of $Bi(NO_3)_3 \cdot 5H_2O$ and varying quantities of $CuCl_2$ (0 mg, 200 mg, 400 mg, 600 mg, and 800 mg) were uniformly dispersed in 50 mL of deionized water. Subsequently, 0.48 g of CH_4N_2O, 2.35 g of $C_6H_5Na_3O_7 \cdot 2H_2O$, and 0.4 g of $C_{19}H_{42}BrN$ were added to the mixture. The resulting solution was stirred for 30 minutes, and the pH value of the solution was adjusted to 7 using a NaOH and HNO_3 solution under stirring. The homogeneous mixture was then transferred into a Teflon-lined stainless-steel autoclave (100 mL capacity) and maintained at 200°C for 24 hours. After the reaction, the products were recovered through centrifugation and washed several times with absolute ethanol and deionized water. The purified products were subsequently dried at 60°C for 12 hours. The dried precursor was calcined in a muffle furnace at 250°C for 1 hour. The heterostructured samples are denoted as Cux-BC (x =

10, 20, 30, 40), where x represents the nominal Cu precursor loading, defined as the mass ratio of $CuCl_2$ to $Bi(NO_3)_3 \cdot 5H_2O$ adjusted to approximately 10, 20, 30, and 40 wt%, respectively. The sample labeled BC corresponds to 0 wt% $CuCl_2$ and thus consists of pristine $Bi_2O_2CO_3$ without CuO decoration.

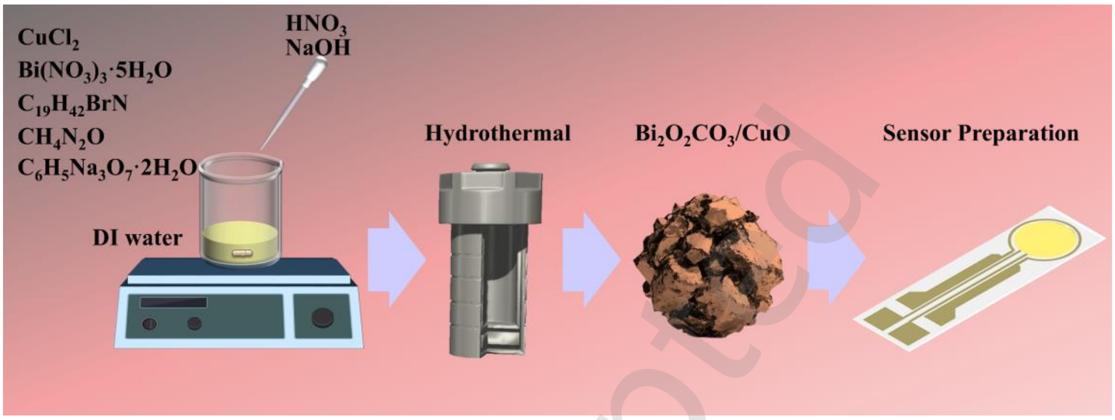

Fig. 1. Schematic illustrations of the fabrication process of Cux-BC microstructure.

2.3 Characterization

The structural and phase composition of the synthesized materials was characterized by X-ray diffraction (XRD) using a Bruker D8 Advance diffractometer. Surface morphology was examined via field-emission scanning electron microscopy (FE-SEM, S4800) and high-resolution transmission electron microscopy (HRTEM, Tecnai). Fourier transform infrared (FT-IR) spectra were recorded on an Agilent 660-IR spectrometer using the KBr pellet method. Optical absorption and band gap values were evaluated using a Cary 5000 UV-Vis-NIR spectrophotometer (Varian, USA). X-ray photoelectron spectroscopy (XPS, Thermo Fisher ESCALAB250Xi) and high-angle annular dark-field scanning transmission electron microscopy (HAADF-STEM) combined with energy-dispersive spectroscopy (EDS) were employed to analyze elemental composition and chemical states. The C 1s peak at 284.8 eV was used as an internal standard for XPS calibration. Electron paramagnetic resonance (EPR) spectroscopy (Bruker A300-10/12) was used to detect surface O_V. The specific surface area and pore structure were determined using the Brunauer–Emmett–Teller (BET) method with an Autosorb IQ3 analyzer (Quantachrome Instruments). Thermogravimetric analysis (TGA, Pyris 1 TGA, PerkinElmer, USA) was conducted under an oxygen atmosphere with a heating rate of 10.00ºC/min to assess thermal stability. Volatile compounds were extracted using headspace solid-phase microextraction (HS-SPME) and analyzed via gas chromatography-mass–mass spectrometry (GC-MS, Trace ISQ, Thermo Fisher, USA). A fused-silica fiber coated with DVB/CAR/PDMS (50/30 μm, Supelco, Bellefonte, PA, USA) was employed for SPME. Cooked rice samples (20 g) were sealed in 20 mL vials with PTFE/silicone septa, incubated at 50°C for 60 minutes, and then the fiber was thermally desorbed at 250ºC for 5 minutes in the GC injection port. Volatile separation was achieved using a DB-5MS capillary column (30 m × 0.25 mm × 0.25 μm) in splitless mode with a carrier pressure of 6 psi. The oven temperature was programmed as follows: 40°C for 5 minutes, ramped to 125°C at 8°C/min (held for 3 minutes), then to 165°C at 4°C/min (held for 3 minutes), and finally to 250°C at 3°C/min (held for 2 minutes). This non-uniform temperature program was adapted and optimized in preliminary experiments to achieve baseline separation of benzaldehyde, nonanal and 1-octen-3-ol while maintaining a reasonable analysis time and ensuring complete elution of higher-boiling matrix components. Mass spectra were acquired in electron ionization mode at 70 eV, with an ion source temperature of 250°C, a multiplier voltage of 1000 V, and a scan range of 20-400 m/z. Compound identification was based on spectral matching with the NIST 11 and WILEY 07 libraries, as well as retention index (RI) comparison against a series of n-alkane standards (C7-C40).

2.4 Gas Sensor Equipment

The gas sensing chips consisted of commercial alumina substrates (6 × 30 mm) pre-patterned with screen-printed platinum heaters and gear-shaped measurement electrodes (electrode gap: 0.42 mm). These substrates were purchased from Wuhan Huachuang Ruike Technology Co., LTD. and used as received. No further optimization of the electrode geometry was performed, as the focus of this study is on the Cux-BC sensing layer. The prepared sensor substrates were ultrasonically cleaned in deionized water and absolute ethanol. Specifically, fixed milligram of synthetic gas-sensitive powder material was dispersed in deionized water or absolute alcohol to form a homogeneous slurry, which was then uniformly drop coated onto the substrates. The coated substrates were dried and thermally treated in an electric heating forced-air oven to obtain stable sensor elements suitable for subsequent gas-sensing measurements. The gas sensing measurement setup comprised four channels with programmable temperature control which was purchased from Wuhan Huachuang Ruike Technology Co., LTD. To prepare for gas sensing tests, the sensors, after film coating, were preheated for approximately 10 hours at 200°C and then stabilized at the testing temperatures under a flow of high-purity air (79% N_2 + 21% O_2) for 3-5 hours to achieve a stable resistance baseline. The mass flow controllers (MFC) were applied to regulate the standard VOC concentration and the high-purity mixed air (Nanjing Special Gas Factory Co., Ltd.). Data were recorded using a desktop computer equipped with an analog-to-digital (A/D) converter and a laboratory DC power supply (GPS-3303C), monitoring the electrical resistance across the channels. All tests were performed at room temperature (25 ± 2°C) and the mean relative humidity was approximately 15-20%. The sensor response is expressed as R_a/R_g, where R_a and R_g denote the resistance in the presence of air and the target gas, respectively. The response and recovery time indicated the time needed for the response to change by 90% during the exposure and removal stages of the target gas, respectively. The saturated vapor pressures of benzaldehyde, nonanal, and 1-octen-3-ol liquids are 0.975 mmHg, 0.26 mmHg, and 0.75 mmHg at room temperature, respectively. The concentrations of VOC gases were calculated through Equation (1) [38] and the concentration of injected VOC (in ppm) in testing was adjusted by the flowmeters.

$$\text{Concentration of VOCs (ppm)}=(\text{vapor pressure of VOCs(mmHg)}/760)\times 10^6 \quad (1)$$

Results and discussion

3.1 Structural and Morphological Characterizations

XRD analysis was performed to determine the composition and structural properties of the synthesized products, as well as to evaluate changes in composition under varying synthesis conditions. As shown in Fig. 2a, the pristine BC sample exhibits a crystalline phase consistent with orthorhombic $Bi_2O_2CO_3$ (JCPDS No. 84-1752), characterized by three prominent diffraction peaks at 23.9°, 30.3°, and 32.7°, corresponding to the (121), (161), and (002) crystal planes, respectively. Following the addition of $CuCl_2$ at the metal basis grade during the synthesis process, two additional peaks emerged in the XRD diffractogram of the resultant sample, located approximately 36.6° and 43.6°, which are attributable to the (111) and (200) crystal planes of the cubic CuO structure (JCPDS No. 78-0428). Notably, the peak corresponding to the (200) crystal plane of the CuO phase has shifted to a higher angle compared to the standard PDF card. This shift indicates lattice compression, suggesting that CuO has a smaller lattice constant ($a = b = c = 4.245$ Å) compared to the substrate material, BC, which has lattice constants of $a = c = 5.468$ Å and $b = 27.320$ Å. As the amount of $CuCl_2$ in the synthesis gradually increases from 200 mg to 800 mg, the intensity of the peak corresponding to the CuO (200) crystal also increases, confirming the successful formation of the CuO/BC p-n heterostructure.

The morphology of the Cu20-BC sample was examined using scanning electron microscopy (SEM) and transmission electron microscopy (TEM) techniques. As illustrated in Fig. 2b, Cu20-BC exhibits a micro-flower structure with semi-hollow characteristics, which is further confirmed by the TEM images (Fig. 2c-2e). Such a semi-hollow micro-flower architecture is expected to provide a larger effective surface area, more exposed Cu-BC interfaces, and interconnected diffusion pathways for VOC molecules, which is beneficial for improving gas-sensing sensitivity as well as response and recovery behavior. Additionally, defects within the Cu20-BC structure are clearly visible in the high-resolution transmission electron microscopy (HRTEM) lattice fringe image (Fig. 2f), verifying the presence of defects in the structure of the Cu20-BC sample. The selected area electron diffraction (SAED) pattern (Fig. 2g) indicates the single-crystalline nature of the Cu20-BC sample. Furthermore, as shown in Fig. 2h-2n, the energy-dispersive X-ray spectroscopy (EDS) elemental mapping reveals a uniform distribution of Bi, C, O, and Cu elements throughout the Cu20-BC micro-flower sample.

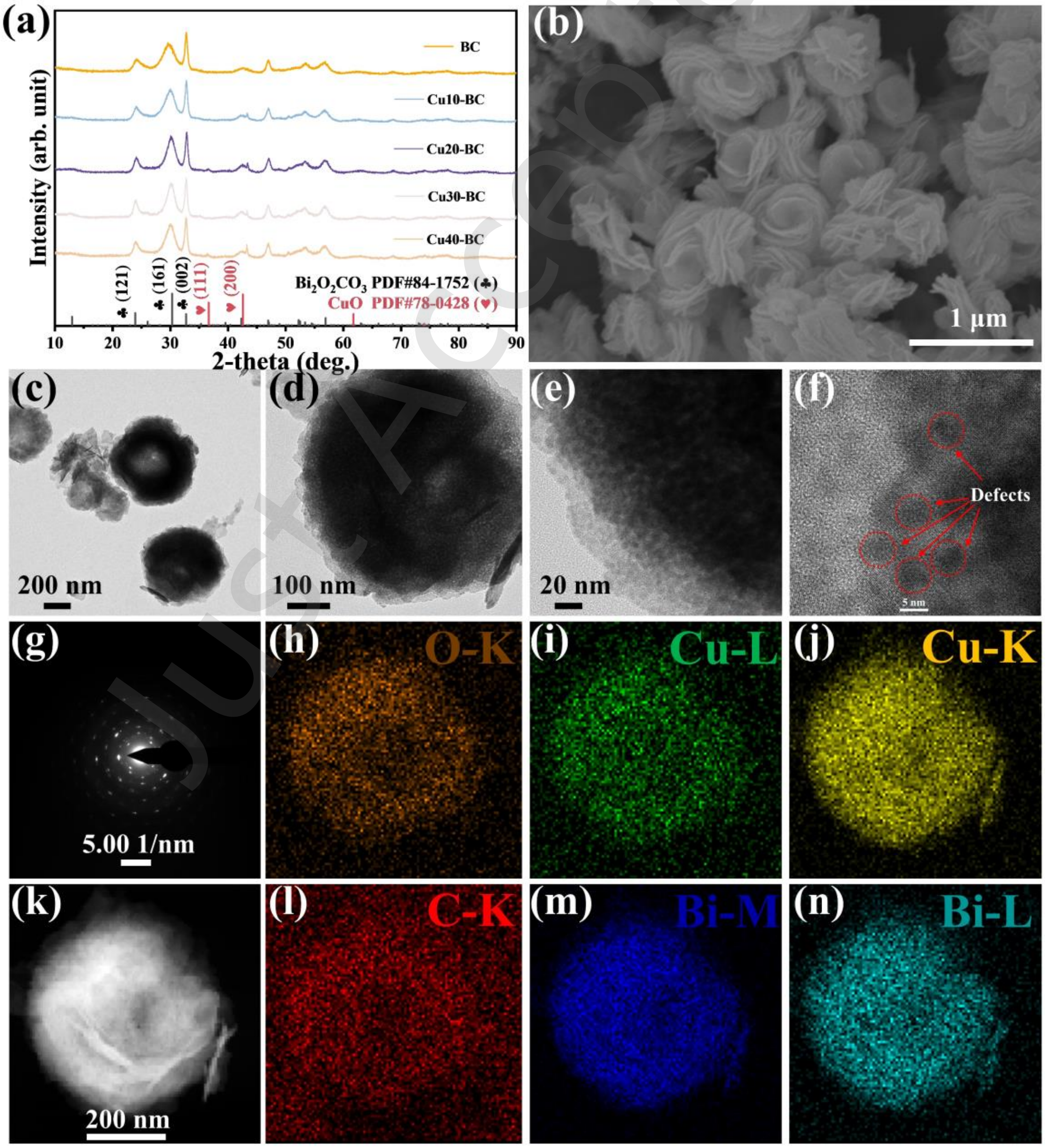

Fig. 2. (a) XRD patterns of BC, Cu10-BC, Cu20-BC, Cu30-BC, and Cu40-BC samples, (b) SEM images of the Cu20-BC sample, (c-e) TEM images of the Cu20-BC sample, (f) HRTEM image of defective sites of Cu single atom in the Cu20-BC sample, (g) SAED pattern of the Cu20-BC sample, (h-j, l-n) EDS elemental mapping images of O, Cu, C, and Bi, (k) HAADF-STEM image of the Cu20-BC sample.

The XPS analysis was conducted to investigate the surface chemical composition and elemental states, as shown in Fig. 3. Cu20-BC was chosen as the representative CuO/BC heterostructure for detailed XPS analysis because it exhibits the highest VOC sensing response and the largest O_V concentration among the Cux-BC series, as evidenced by the EPR and gas sensing results (Figs. 4b and 6e-g). The presence of Bi, C, Cu, and O in the Cu20-BC sample was confirmed (Fig. 3a). The O 1s spectrum of Cu20-BC, shown in Fig. 3b, reveals three components centered at 528.9 eV (lattice oxygen, O_L), 529.9 eV (O_V), and 531.6 eV (chemisorbed oxygen species, O_C) [39]. Comparative analysis of the O_V component derived from the deconvolution of the O 1s spectra indicates a significantly higher concentration of O_V (53.8%) in Cu20-BC compared to pristine BC (42.3%). This increase in O_V suggests that lattice mismatch induces alterations in the spatial distribution of electrons or ions within Cu20-BC, leading to the formation of excess O_V. And the establishment of a p-n heterostructure may enhance the sensing properties, as the vacancy sites could facilitate oxygen adsorption [40, 41]. Additionally, a comparison of the Bi 4f peak in Cu20-BC shows a narrowing effect relative to pure BC samples (Fig. 3c). This phenomenon can be attributed to the reorganization of electronic states at the CuO and BC interface, resulting in increased localization of electrons within the valence and conduction bands. The C 1s spectrum of Cu20-BC (Fig. 3d) was deconvoluted into two distinct components: one centered at 284.1 eV corresponds to adventitious carbon (AC) species, while the one centered at 287.9 eV is associated with ester groups. These observations are consistent with the C 1s spectrum recorded for the BC sample [42, 43].

The Cu 2p spectrum indicates the presence of the Cu^{2+} oxidation state, as confirmed by Fig. 3e. The presence of Cu^{+} $2p_{3/2}$ and Cu^{+} $2p_{1/2}$ peaks suggests that Cu^{2+} is partially reduced to Cu^{+} due to the presence of O_V in the samples. In a related study, Wang et al. demonstrated that the addition of $CuCl_2$ during material modification successfully stabilized single-atom Cu on ultrathin $WO_{2.72}$ nanowires, achieving high-sensitivity detection of toluene [32], as we have successfully loaded CuO, primarily due to the differences in the properties of the support and the varying amounts of copper loaded.

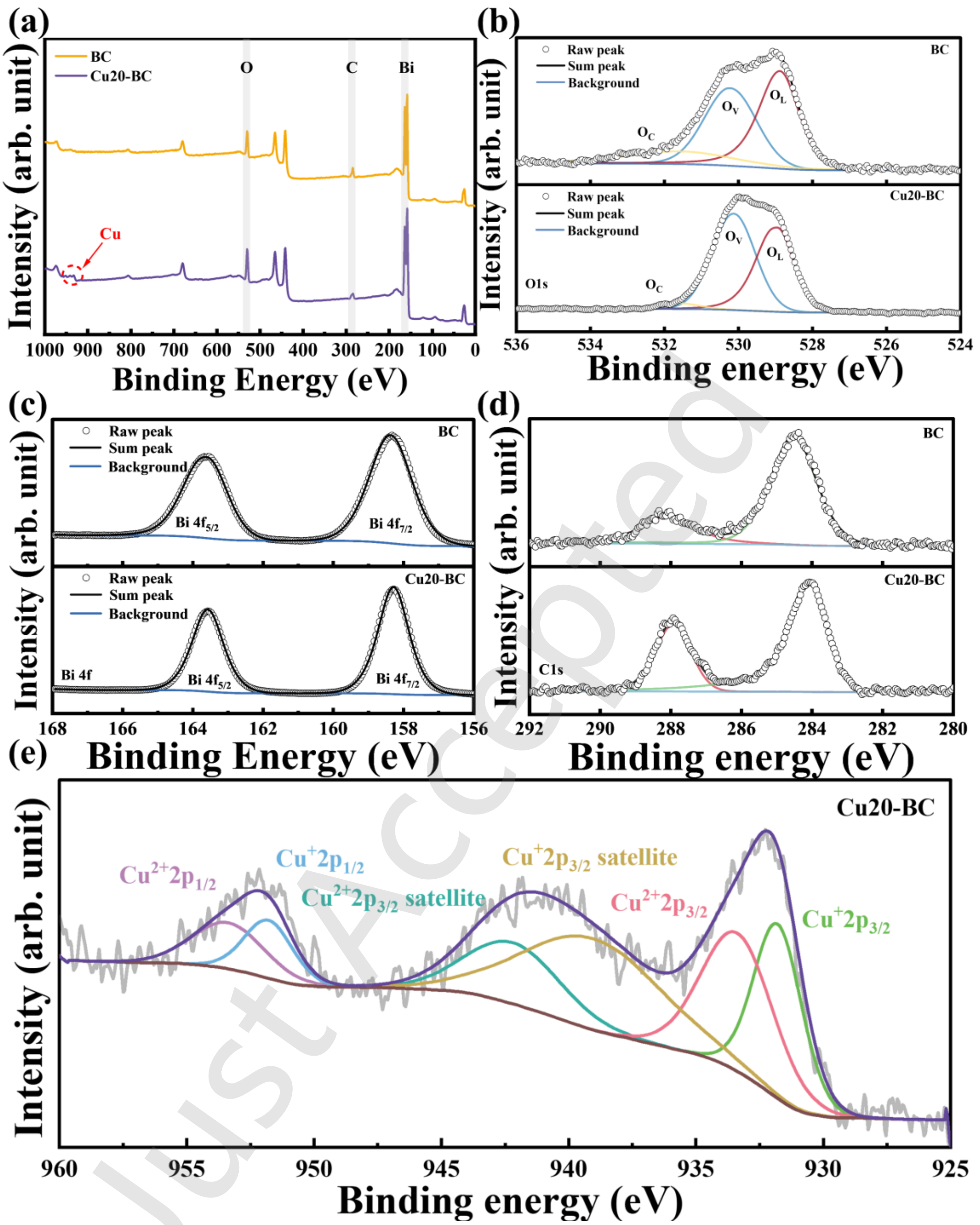

Fig. 3. (a) XPS survey scan and core-level spectra of (b) O 1s, (c) Bi 4f, (d) C 1s, and (e) Cu 2p regions.

FT-IR spectroscopy was employed to examine the structural bonding associated with functional groups. As illustrated in Fig. 4a, the absorption band at 851 cm^{-1} corresponds to the out-of-plane bending modes of CO_3^{2-}. Additionally, the bands at

1386 cm^{-1} and 1532 cm^{-1} are assigned to the antisymmetric vibrational modes of CO_3^{2-} [44]. To further investigate and confirm the presence of O_V, electron paramagnetic resonance (EPR) spectra were conducted on the as-prepared samples. The EPR signal can be attributed to paramagnetic O_V, which create intermediary energy levels within the band gap. As illustrated in Fig. 4b, the EPR signal at a g factor of 2.003 is detected in the as-prepared samples, corresponding to unpaired electrons in O_V sites, thereby confirming the existence of O_V. Furthermore, the signal intensity increased in the following order: Cu20-BC > Cu30-BC > Cu10-BC > Cu40-BC > BC, with Cu20-BC exhibiting the highest content of O_V. Additionally, the calculated intensity signal in Fig. 4c exhibits asymmetric characteristics, which are related to the localization of the defect center on the surface. The UV-Vis absorption spectra of all samples were obtained, as shown in Fig. 4d. The bandgap of the BC and Cu20-BC were calculated to be 2.79 eV and 2.47 eV, respectively, according to the Tauc equation (Fig. 4e). A reduced band gap indicate that it is easier to excite electrons into the conduction band, thereby enhancing the conductivity of the material and improving the responsiveness to gas molecules. The thermal stability of Cu20-BC was investigated using thermogravimetric analysis (TGA) (Fig. 4f and 4g), which shows two stages of large mass losses corresponding to the evaporation of adsorbed water (1.01 wt%) and the release of CO_2 during decomposition (8.93 wt%) of the sample, respectively. The Brunauer-Emmett-Teller (BET) results for BC and Cu20-BC are shown in Figs. 4h and 4i. The successful formation of a heterostructure in Cu20-BC, characterized by a greater abundance of Ov, leads to an increased BET surface area (76.667 $m^2 \cdot g^{-1}$), compared to the BC sample (BET surface area: 13.069 $m^2 \cdot g^{-1}$). Specifically, the loading of CuO induces the reorganization of the BC framework, resulting in the formation of a hollow structure and an increase in the specific surface area. Furthermore, the loaded CuO provides more active sites, significantly enhancing the material's adsorption capacity for gases and effectively increasing the utilization of the surface area. During the process of loading CuO, the growth of BC particles is promoted, resulting in their aggregation into smaller units, which further increases the specific surface area of the material. To further clarify the origin of the reduced band gap in Cu20-BC, we correlated the optical, defect and porosity results. The narrowing of the band gap from 2.79 eV (BC) to 2.47 eV (Cu20-BC) (Fig. 4e) is consistent with the higher O_V content, as indicated by the larger O_V contribution in the O 1s XPS spectra, the stronger EPR signal at $g = 2.003$, and the defect-rich lattice regions observed in the HRTEM image (Fig. 2f). These features suggest the introduction of additional defect states within the band gap. At the same time, BET analysis shows that Cu20-BC possesses a much larger specific surface area and more open pores than pristine BC, reflecting a CuO-induced reconstruction into a semi-hollow, porous micro-flower architecture. Therefore, the reduced band gap, increased defect density and enhanced porosity can be ascribed to the same structural modification process and jointly contribute to the improved VOCs sensing performance of the Cu20-BC sample.

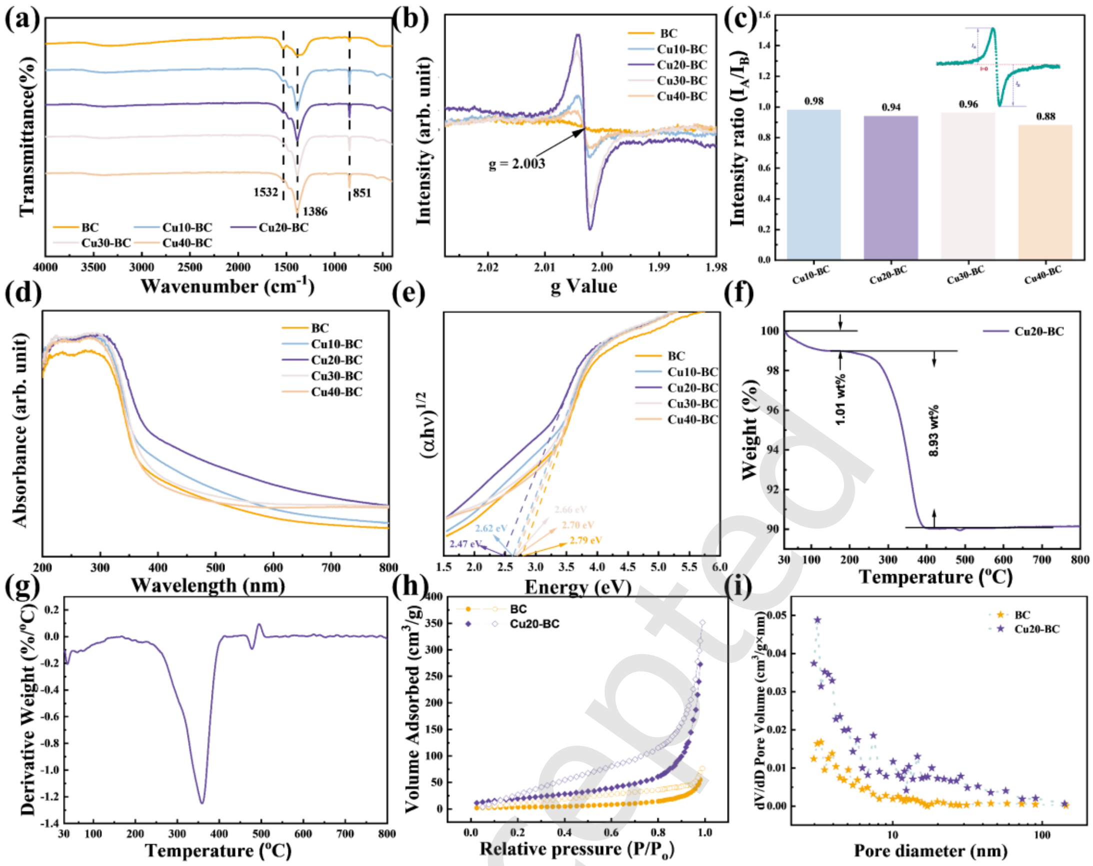

Fig. 4. (a) FT-IR spectrum of all samples, (b) EPR spectra of all samples, (c) intensity ratio of symmetry parameters of defect signal. The ratio of symmetry coefficients is defined as I_A/I_B, (d) UV-Vis absorption spectra of all samples, (e) Tauc plots of all samples, (f) TGA curves for Cu20-BC, (g) derivatives of the TGA curves for Cu20-BC, (h) N_2 adsorption-desorption isotherms, and (i) pore-size distributions of BC and Cu20-BC.

3.2 Gas Sensing Properties

To assess the potential of the as-fabricated sensor array in evaluating the quality of cooked rice, we first verified the presence of VOCs released from cooked rice (raw materials, including fresh uncooked rice and uncooked rice stored for six months) by conducting headspace solid-phase microextraction (HS-SPME) combined with gas chromatography-mass spectrometry (GC-MS). As shown in Fig. 5a, the presence of benzaldehyde and nonanal was confirmed in cooked rice prepared from grains under fresh conditions, while benzaldehyde, nonanal, and 1-octen-3-ol were detected in cooked rice prepared from grains stored for six months. Additionally, the mass spectra of the benzaldehyde, nonanal, and 1-octen-3-ol in cooked rice made from grains stored for six months are depicted in Fig. 5b.

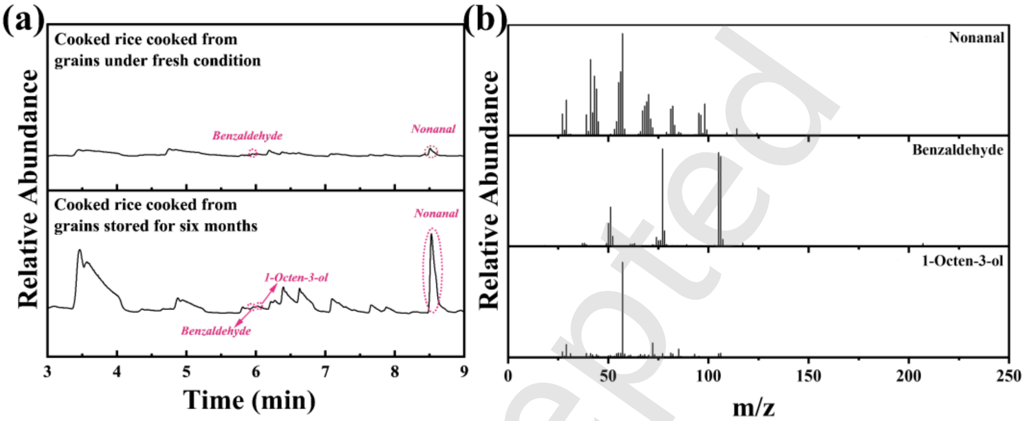

Fig. 5. (a) Chromatogram of a representative cooked rice cooked from grains under fresh conditions and cooked rice prepared from grains stored for six months, (b) mass spectra of the benzaldehyde, nonanal, and 1-octen-3-ol in cooked rice prepared from grains stored for six months.

For the specific VOCs sensing process, we initially employed a single sensor (Cux-BC, x = 10, 20, 30, and 40) to detect the benzaldehyde, nonanal, and 1-octen-3-ol gases at room temperature. The transient response features for VOCs were observed in all sensors, as shown in Fig. 6a. A good linear correlation was established between the sensor response and the concentration of the detected gas, demonstrating its practical applicability (Fig. 6b-6d). Among the response values, Cu20-BC exhibited the highest response values for the three gases, with the specific order of response values being Cu20-BC > Cu30-BC > Cu10-BC > Cu40-BC (Fig. 6e-6g). In the Cu-BC heterostructure, moderate loading of CuO enhances the gas sensing response of the material. This improvement is primarily achieved through promoting interface contact, improving electrical conductivity, increasing surface activity, and forming an appropriate conductive network. An optimal amount of copper oxide can modulate the surface electronic structure, thus enhancing the responsiveness to three VOCs. Conversely, excessive loading may lead to adverse effects. Therefore, optimizing the loading of copper oxide is crucial for enhancing gas sensing performance, with Cu20-BC identified as the optimal sensing material for this study. In Figs. 6h-6k, the pattern recognition treated by the principal component analysis (PCA) method demonstrated the exclusive detection of all sensors for benzaldehyde, nonanal, and 1-octen-3-ol, where three clearly separated point in the PCA score plots indicate good selectivity among these VOCs.

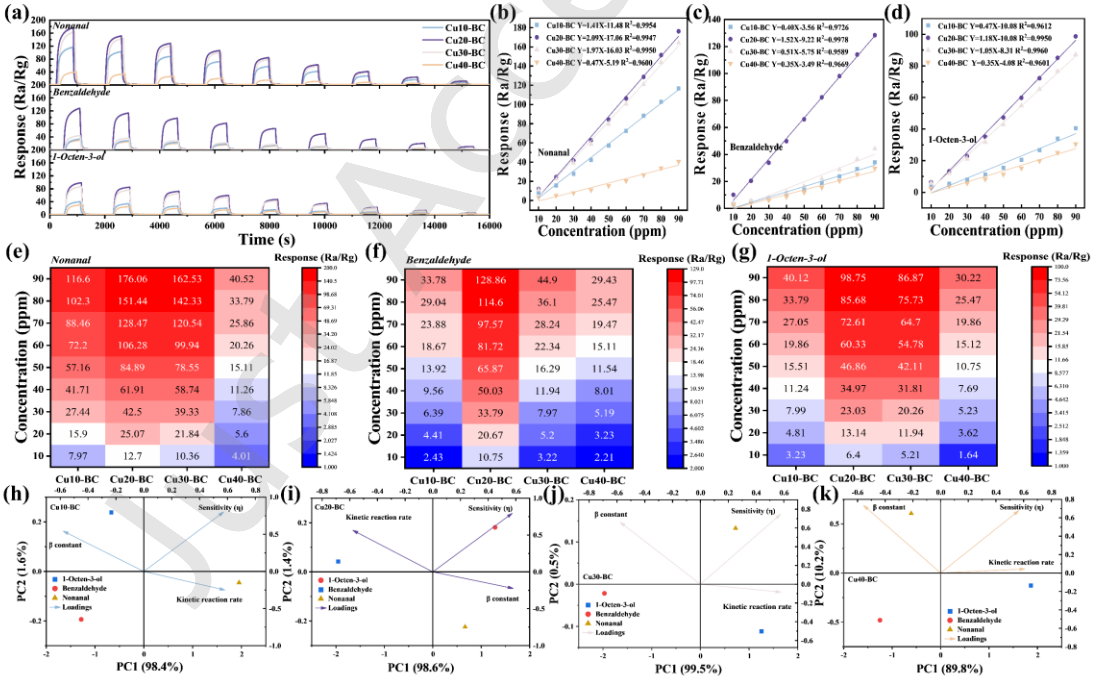

Nonanal

Concentration (ppm)	Cu10-BC	Cu20-BC	Cu30-BC	Cu40-BC
90	116.6	176.06	162.53	40.52
80	102.3	151.44	142.33	33.79
70	88.46	128.47	120.54	25.86
60	72.2	106.28	99.94	20.26
50	57.16	84.89	78.55	15.11
40	41.71	61.91	58.74	11.26
30	27.44	42.5	39.33	7.86
20	15.9	25.07	21.84	5.6
10	7.97	12.7	10.36	4.01

Benzaldehyde

Concentration (ppm)	Cu10-BC	Cu20-BC	Cu30-BC	Cu40-BC
90	33.78	128.86	44.9	29.43
80	29.04	114.6	36.1	25.47
70	23.88	97.57	28.24	19.47
60	18.67	81.72	22.34	15.11
50	13.92	65.87	16.29	11.54
40	9.56	50.03	11.94	8.01
30	6.39	33.79	7.97	5.19
20	4.41	20.67	5.2	3.23
10	2.43	10.75	3.22	2.21

1-Octen-3-ol

Concentration (ppm)	Cu10-BC	Cu20-BC	Cu30-BC	Cu40-BC
90	40.12	98.75	86.87	30.22
80	33.79	85.68	75.73	25.47
70	27.05	72.61	64.7	19.86
60	19.86	60.33	54.78	15.12
50	15.51	46.86	42.11	10.75
40	11.24	34.97	31.81	7.69
30	7.99	23.03	20.26	5.23
20	4.81	13.14	11.94	3.62
10	3.23	6.4	5.21	1.64

Fig. 6. (a) Transient response of Cux-BC (x = 10, 20, 30, and 40) film to nonanal, benzaldehyde, and 1-octen-3-ol (10-90 ppm) at room temperature, concentration-dependent response curves of the fabricated sensors for (b) nonanal, (c) benzaldehyde, and (d) 1-octen-3-ol, response values of fabricated sensors to different concentrations

of (e) nonanal, (f) benzaldehyde, and (g) 1-octen-3-ol at room temperature (10-90 ppm), pattern recognition by the PCA method to analyze the exclusive detection of the (h) Cu10-BC, (i) Cu20-BC, (j) Cu30-BC, and (k) Cu40-BC sensors, respectively.

3.3 Gas Sensing Mechanism

To investigate the enhanced sensing mechanism, we construct the band structures of BC and Cu20-BC according to the following process. Firstly, the valence band potentials (E_{VB}) for BC and Cu20-BC were determined to be 0.69 eV and 1.00 eV, respectively, using the valence band X-ray photoelectron spectroscopy (VB-XPS) technique (Fig. 7a). By applying Equation (2), the valence band potential relative to the standard hydrogen electrode ($E_{VB,\ NHE}$) of BC and Cu20-BC is 0.77 eV and 1.08 eV, respectively [45],

$$E_{VB,\ NHE}=\varphi+E_{VB,\ XPS}-4.44 \qquad (2)$$

where φ is the instrument work function (4.52 eV), and $E_{VB,\ XPS}$ is the valence band potential. Secondly, the correlation between the work function in the actual sensing process (Φ) and the contact potential discrepancy (ΔV) is based on Equation (3) [46],

$$\Delta V=\Phi-\varphi \qquad (3)$$

where ΔV represents the interval between two different inflection points (IP) on the graph, as depicted in Figs. S1 and S2. Consequently, the Φ for BC and Cu20-BC were obtained to be 5.59 eV and 5.17 eV, respectively. Finally, the band structure can be obtained, as shown in Fig. 7b. The lower work function facilitates the transfer of electrons from VOC molecules to the Cu20-BC sensor surface, thereby increasing the sensor's sensitivity to detect lower concentrations of VOC molecules. Sensors with lower work functions require less energy to initiate the sensing, enabling more energy-efficient sensor operation and making sensing at room temperature possible, which is important for portable and wearable sensor applications.

The heterostructure formed by BC and CuO demonstrates significantly enhanced performance in VOC gas sensing detection. Its primary mechanisms can be summarized as follows (Fig. 7c). First, the formation of the heterostructure increases the interfacial contact between the two materials and promotes effective separation and migration of charge carriers, allowing photogenerated electrons and holes to be separated at the interface, thus reducing carrier recombination and improving the conductivity. Secondly, the structure significantly increases the number of surface-active sites, enhancing the contact between gas molecules and sensing materials, which improves the adsorption capacity and reactivity of VOCs. Furthermore, the band structure of the heterostructure is adjusted, reducing the energy barrier required for the reaction of gas molecules, thereby enhancing sensitivity to VOCs. Additionally, the catalytic properties of CuO play a crucial role, accelerating chemical reactions and enhancing the response speed of sensors. Collectively, these factors highlight the advantages of Cu-BC heterostructure in gas sensing detection. In detail, taking nonanal as a representative example, when Cu-BC is exposed to air, oxygen molecules are first adsorbed onto its surface and capture electrons from the conduction band, forming chemisorbed oxygen ions. At temperatures below 150°C, these species mainly exist in the form of O_2^-. The corresponding processes are described by Equations (4) and (5) [47, 48]. When the sensor is subsequently exposed to nonanal, a reducing gas, the nonanal molecules react with the adsorbed O_2^- species and release electrons back into the conduction band of Cu-BC. This process shrinks the electron depletion layer and lowers the potential barrier at the grain boundaries, as outlined in Equations (6) and (7) [49, 50]. As a result, the resistance of the Cu-BC gas sensor decreases, while $C_9H_{18}O$ reacts with O_2^- to form $C_9H_{16}O$ and is ultimately oxidized to CO_2 and H_2O [51, 52].

$$O_2(gas) \rightarrow O_2\ (ads) \quad (4)$$

$$O_2(ads) + e^- \rightarrow O_2^-\ (ads) \quad (5)$$

$$C_9H_{18}O(g) \rightarrow C_9H_{18}O\ (ads) \quad (6)$$

$$2C_9H_{18}O(ads) + O_2^-(ads) \rightarrow 2C_9H_{16}O(ads) + 2H_2O(g) + e^- \quad (7)$$

To further investigate the adsorption and diffusion mechanisms of the target gas molecules and oxygen on the surface of materials, molecular dynamics (MD) simulations were employed. The geometric structures of BC were acquired following the construction of the (020) $Bi_2O_2CO_3$ surface with a 25 Å thick vacuum layer while the geometric structures of Cu-BC were acquired following the construction of the (020) $Bi_2O_2CO_3$ surface and (100) CuO surface with a 25 Å thick vacuum region along the surface normal, which was introduced to avoid spurious interactions between periodically repeated slabs and to ensure a converged surface dipole and electrostatic potential profile. This vacuum layer does not directly modify the intrinsic band alignment of the $CuO/Bi_2O_2CO_3$ p-n junction, but it electrostatically isolates the slab so that the band bending, depletion layer width, and gas-induced surface potential changes arise solely from the heterointerface and the adsorbed VOC or O_2 species, rather than from artificial interactions between periodic images. In Figs. 7e-f, as nonanal gradually approaches the material surface and O_2 molecules diffuse simultaneously, a shift in adsorption kinetics is observed for both BC and Cu-BC systems. This transition aligns well with the previously proposed model of oxygen adsorption. As depicted in Fig. 7d, between 1 ps and 25 ps, the interaction energy (E_{int}) in both BC and Cu-BC systems decreases significantly, indicating that nonanal is approaching the surface and entering the attractive interaction region, primarily driven by van der Waals forces. Interestingly, after 50 ps, although the calculated E_{int} of nonanal and O_2 molecules on the CuO-loaded $Bi_2O_2CO_3$ heterojunction are slightly lower in absolute value compared to pristine

$Bi_2O_2CO_3$, the gas-sensing response is significantly enhanced, as depicted in Fig. 6a. This seemingly counterintuitive result can be attributed to several factors. Firstly, the formation of a p-n heterojunction between p-type CuO and n-type $Bi_2O_2CO_3$ facilitates efficient charge separation and modulates the depletion layer width, amplifying the surface potential change upon gas exposure. Secondly, moderate adsorption strength is more favorable for reversible gas adsorption-desorption dynamics, ensuring faster response and recovery. Finally, the CuO domains provide additional active sites for oxygen activation and catalytic oxidation of nonanal, thereby enhancing electron transfer and signal output. These synergistic effects highlight the critical role of interface engineering in modulating both adsorption thermodynamics and charge transport behavior, providing a rational approach for designing high-performance gas sensors.

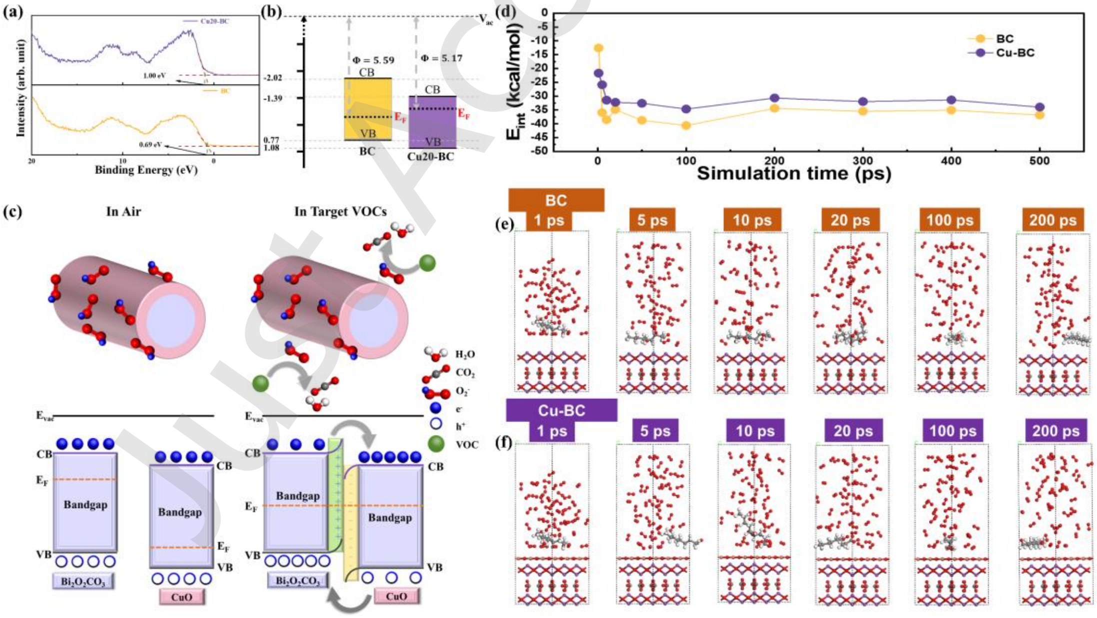

Fig. 7. (a) VB-XPS and (b) band structure of Cu20-BC and BC. (c) Schematic illustration of the nonanal, benzaldehyde, and 1-octen-3-ol sensing mechanism of Cu-BC micro-flowers at room temperature. (d) E_{int} for the dynamic process of nonanal and oxygen diffusion on BC and Cu-BC, and the corresponding MD simulation snapshots

of (e) BC and (f) Cu-BC.

3.4 Sensor arrays detection

Fig. 8 illustrates the overall construction of a real-time gas sensor array and the evaluation of cooked rice quality performance. A schematic diagram of the system structure, which includes a circuit board, a microcontroller unit (MCU), and a data transmission module, enables an integrated and portable gas detection function, as shown in Fig. 8a. The MCU sequentially reads the real-time signal from the four channels based on Cu10-BC, Cu20-BC, Cu30-BC, and Cu40-BC materials reported above. A physical photograph of the sensor circuit board in the system, as shown in Fig. 8b, displays the layout and compact design of the multi-channel gas sensor module. The correlation curve between voltage and resistance in the sensing channel one is demonstrated in Fig. 8c, reflecting the correlation between voltage and resistance, which indicates the stability of the sensing system. To assess the potential of the gas sensor array in evaluating the quality of agricultural products, we studied the changes in VOC concentration emitted from various cooked rice samples (uncooked rice with different storage times) of similar weights (≈approximately 20 g). VOCs detection on cooked rice prepared from coarse rice with different storage times (0, 1, 2, 3, 4, 5, and 6 weeks) was performed using homemade equipment with a real-time gas sensor array. The data were obtained, and we employed two dimensionality reduction methods (PCA and linear discriminant analysis (LDA)) to visualize the dynamic loop data for cooked rice detection (Fig. 8d-e). It can be observed that there is considerable overlap among the data point regions of cooked rice made from raw rice stored for 0 to 2 weeks (Fig. 8d). Similar analysis results were obtained in Fig. 8e. In comparison, the three groups (fresh group (0-2 weeks): mild group (3-4 weeks) and moderate group (5-6 weeks)) were almost distinct. This clear grouping in both PCA and LDA score plots further confirms the selectivity of the sensor array toward different conditions of cooked rice in complex VOC environments. Furthermore, the VOCs detection data of cooked rice made from rice with different storage times exhibited specific patterns and trends, allowing clear differentiation of the data sets for varying storage durations, thereby providing an innovative strategy for detecting grain and other agricultural products.

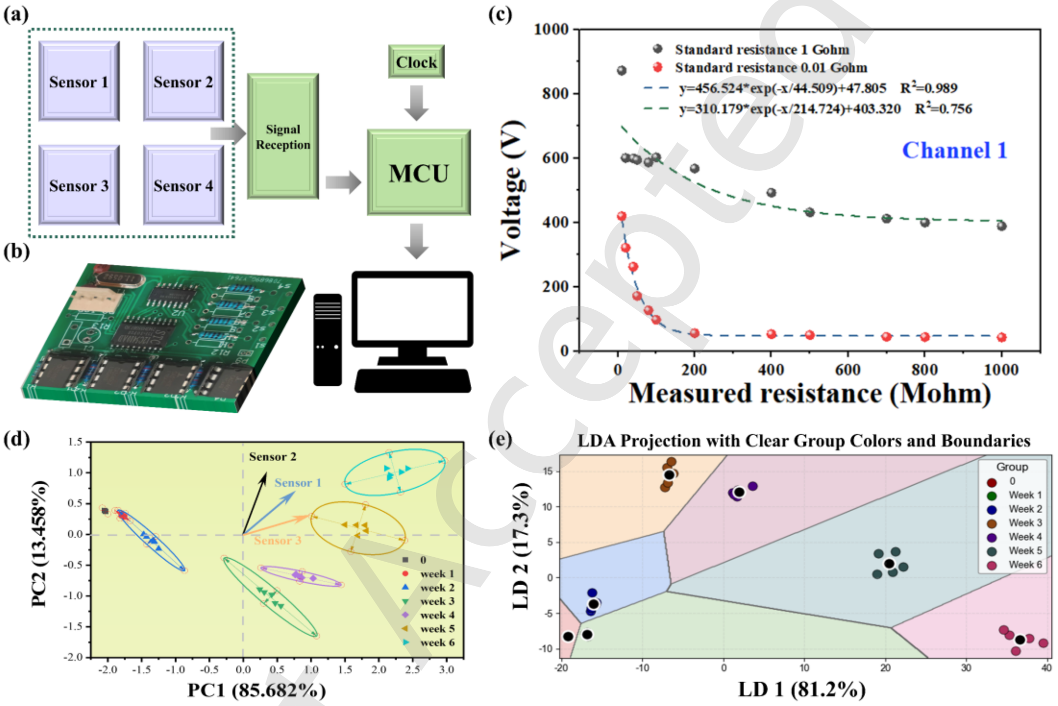

Fig. 8. (a) Schematic of the real-time gas sensor array. (b) Photograph of the sensor PCB of the real-time gas sensor array. (c) The relationship between voltage and measured resistance for channel one in the gas sensor array. (d) Two-dimensional score plots of the first principal components derived from response curves for volatile gas detection on cooked rice cooked from fresh grains and grains stored for different weeks using a real-time gas sensor array, (e) LDA pattern recognition of volatile gas detection on cooked rice cooked from fresh grains and grains stored for different weeks using real-time gas sensor array.

Conclusion

In conclusion, this study demonstrates a facile one-step hydrothermal route followed by mild calcination to prepare BC-based p-n heterostructured Cu-BC micro-flowers with controllable CuO loading. By rationally adjusting the $CuCl_2$ content during synthesis, the crystal structure, defect chemistry and semi-hollow micro-flower morphology of BC can be finely tuned, leading to an increased specific surface area, abundant O_V and optimized Cu-BC interfacial contact that are highly beneficial for gas sensing.

Among the prepared samples, Cu20-BC achieves the best balance between CuO loading and structural integrity, and thus delivers markedly enhanced sensitivity toward nonanal, benzaldehyde and 1-octen-3-ol at room temperature, which is attributed to its high concentration of O_V and improved charge transport. On this basis, a portable four-channel sensor array with voltage-resistance conversion circuitry was constructed, enabling real-time, ppm-level detection of VOCs and successful discrimination of cooked rice quality at different storage stages through PCA and LDA.

From a materials-development perspective, the present preparation strategy highlights BC as a versatile Aurivillius-type semiconductor platform. The mild aqueous synthesis, the compatibility with metal oxide decoration and defect engineering, and the capability to form micro-flowers, hollow structures and other morphologies make BC highly attractive for further compositional and structural optimization. Future work can explore cation or anion doping, construction of multi-component heterostructures and integration with microelectromechanical systems or flexible substrates in order to tailor BC-based materials for specific target VOCs, lower detection limits and stable operation under varying humidity and temperature conditions.

Regarding application directions, the Cu-BC platform developed in this work is not limited to the analysis of cooked rice aroma. It can be extended to broader food quality and agricultural scenarios, such as monitoring grain storage, meat and dairy freshness and fermented products, where aldehydes and alcohols are key markers. Combined with machine learning algorithms and wireless communication, BC-based sensor arrays are promising candidates for smart packaging, internet-of-things enabled quality supervision and distributed environmental monitoring of VOCs in indoor air and storage environments. With further miniaturization and integration into wearable or portable formats, BC and its heterostructures are expected to play an increasingly important role in next-generation high-selectivity gas sensing systems for food safety, agriculture and related fields.

Declaration of Competing Interest

The authors declare no competing financial interest.

Acknowledgments

This work was supported by the Outstanding Youth Foundation of Jiangsu Province of China (Grant No. BK20211548), the Yangzhou Science and Technology Plan Project (Grant No. YZ2023246), the Qinglan Project of Yangzhou University, and the China Scholarship Council (Grant No. 202308320445). C.B. is a research associate of the FNRS- Belgium.

References

[1] C. Gonzalez Viejo, S. Fuentes, D.D. Torrico, K. Howell, F.R. Dunshea, Assessment of Beer Quality Based on a Robotic Pourer, Computer Vision, and Machine Learning Algorithms Using Commercial Beers, J. Food Sci. 83 (2018) 1381-1388, https://doi.org/10.1111/1750-3841.14114.

[2] M. Mohd Ali, N. Hashim, S. Abd Aziz, O. Lasekan, Principles and recent advances in electronic nose for quality inspection of agricultural and food products, Trends Food Sci. Technol. 99 (2020) 1-10, https://doi.org/10.1016/j.tifs.2020.02.028.

[3] P.F.M. Pereira, P.H. de Sousa Picciani, V. Calado, R.V. Tonon, Electrical gas sensors for meat freshness assessment and quality monitoring: A review, Trends Food Sci. Technol. 118 (2021) 36-44, https://doi.org/10.1016/j.tifs.2021.08.036.

[4] H.G. Yakubu, Z. Kovacs, T. Toth, G. Bazar, Trends in artificial aroma sensing by means of electronic nose technologies to advance dairy production – a review, Crit. Rev. Food Sci. Nutr. 63 (2022) 234-248, https://doi.org/10.1080/10408398.2021.1945533.

[5] R. Thayil, S.R. Parne, Nanostructured zinc oxide and selenide-based materials for gas sensing application: review, Journal of Materials Science: Materials in Electronics 36 (2025) 322, https://doi.org/10.1007/s10854-025-14401-1.

[6] W. Zhang, Y. Yang, J. Zhang, W. Zheng, Y. Du, B. Dang, Study of the effect of milling on nutritional and sensory quality and volatile flavor compounds of cooked highland barley rice, LWT-FOOD SCIENCE AND TECHNOLOGY 198 (2024), https://doi.org/10.1016/j.lwt.2024.115972.

[7] K. Wimonmuang, Y.-S. Lee, Absolute contents of aroma-affecting volatiles in cooked rice determined by one-step rice cooking and volatile extraction coupled with standard-addition calibration using HS-SPME/GC-MS, Food Chem. 440 (2024), https://doi.org/10.1016/j.foodchem.2023.138271.

[8] W. Jin, Z. Zhang, S. Zhao, J. Liu, R. Gao, P. Jiang, Characterization of volatile organic compounds of different pigmented rice after puffing based on gas chromatography-ion migration spectrometry and chemometrics, Food Res. Int. 169 (2023), https://doi.org/10.1016/j.foodres.2023.112879.

[9] Q. Zhao, J. Xi, X. Xu, Y. Yin, D. Xu, Y. Jin, Q. Tong, L. Dong, F. Wu, Volatile fingerprints and biomarkers of Chinese fragrant and non-fragrant japonica rice before and after cooking obtained by untargeted GC/MS-based metabolomics, Food Biosci. 47 (2022), https://doi.org/10.1016/j.fbio.2022.101764.

[10] K. Wimonmuang, Y.-S. Lee, Absolute contents of aroma-affecting volatiles in cooked rice determined by one-step rice cooking and volatile extraction coupled with standard-addition calibration using HS-SPME/GC–MS, Food Chem. 440 (2024) 138271, https://doi.org/10.1016/j.foodchem.2023.138271.

[11] S. Li, H. Li, L. Lu, G. Shao, Z. Guo, Y. He, Y. Wang, X. Yang, M. Chen, X. Hu, Analysis of rice characteristic volatiles and their influence on rice aroma, Current Research in Food Science 9 (2024) 100794, https://doi.org/10.1016/j.crfs.2024.100794.

[12] Q. Zhao, L. Yousaf, Y. Xue, Q. Shen, Changes in flavor of fragrant rice during storage under different conditions, Journal of the Science of Food and Agriculture 100 (2020) 3435-3444, https://doi.org/10.1002/jsfa.10379.

[13] E. Taghinezhad, A. Szumny, A. Figiel, E. Sheidaee, S. Mazurek, M. Latifi-Amoghin, H. Bagherpour, N. Pachura, J. Blasco, Non-Destructive Determination of Starch Gelatinization, Head Rice Yield, and Aroma Components in Parboiled Rice by Raman and NIR Spectroscopy, Molecules 30 (2025) 2938, https://doi.org/10.3390/molecules30142938.

[14] K. Xu, M. Han, Z. Zheng, Z. Yu, H. Liao, H. Sun, C. Zhang, Well-designed g-C_3N_4 nanosheet incorporated Ag loaded $Er_{0.05}La_{0.95}FeO_3$ heterojunctions for isoamyl alcohol

detection, J. Adv. Ceram. 13 (2024) 736-745, https://doi.org/10.26599/JAC.2024.9220892.

[15] S. Neogi, R. Ghosh, Influence of dipole moment on the VOC sensing properties of $BiFeO_3$ microspheres: Addressing the selectivity towards acetone, Sens. Actuators, B 415 (2024) 135980, https://doi.org/10.1016/j.snb.2024.135980.

[16] M. Souri, H. Salar Amoli, Y. Yamini, Three-dimensionally ordered porous In-doped $SmFeO_3$ perovskite gas sensor for highly sensitive and selective detection of formaldehyde, Sens. Actuators, B 404 (2024) 135213, https://doi.org/10.1016/j.snb.2023.135213.

[17] W. Li, X. Li, Y. Zong, L. Kong, W. Zhu, M. Xu, H. Liu, Detection of n-Propanol Down to the Sub-ppm Level Using p-Type Delafossite $AgCrO_2$ Nanoparticles, ACS Sens. 8 (2023) 289-296, https://doi.org/10.1021/acssensors.2c02182.

[18] X. Li, W. Zeng, S. Zhuo, B. Qian, Q. Chen, Q. Luo, R. Qian, Highly Sensitive Room-Temperature Detection of Ammonia in the Breath of Kidney Disease Patients Using $Fe_2Mo_3O_8/MoO_2@MoS_2$ Nanocomposite Gas Sensor, Adv. Sci. 11 (2024) 2405942, https://doi.org/10.1002/advs.202405942.

[19] K. Liu, Z. Zheng, M. Debliquy, C. Zhang, Highly-sensitive volatile organic compounds evaluation by three-dimensional $ZnFe_2O_4/ZnSnO_3$ heterostructures and their predictive grain quality monitoring, Chem. Eng. J. 453 (2023) 139824, https://doi.org/10.1016/j.cej.2022.139824.

[20] A. Bag, M. Kumar, D.-B. Moon, A. Hanif, M.J. Sultan, D.H. Yoon, N.-E. Lee, A room-temperature operable and stretchable NO_2 gas sensor composed of reduced graphene oxide anchored with MOF-derived $ZnFe_2O_4$ hollow octahedron, Sens. Actuators, B 346 (2021) 130463, https://doi.org/10.1016/j.snb.2021.130463.

[21] X.Y. Huang, K. Chen, W. Xie, Y. Li, F. Yang, Y. Deng, J. Li, F. Jiang, Y. Shu, L.

Wu, W.F. Xie, Y. Deng, Chemiresistive Gas Sensors Based on Highly Permeable Sn-Doped Bismuth Subcarbonate Microspheres: Facile Synthesis, Sensing Performance, and Mechanism Study, Adv. Funct. Mater. 33 (2023), https://doi.org/10.1002/adfm.202304718.

[22] L. Wang, B. Zhang, B. Wang, S. Zeng, M. Zhao, X. Sun, Y. Zhai, L. Xu, In-situ Nano-Crystallization and Solvation Modulation to Promote Highly Stable Anode Involving Alloy/De-alloy for Potassium Ion Batteries, Angew. Chem. Int. Ed. 60 (2021) 15381-15389, https://doi.org/10.1002/anie.202100654.

[23] H. Lu, L. Xu, B. Wei, M. Zhang, H. Gao, W. Sun, Enhanced photosensitization process induced by the p–n junction of $Bi_2O_2CO_3$/BiOCl heterojunctions on the degradation of rhodamine B, Appl. Surf. Sci. 303 (2014) 360-366, https://doi.org/10.1016/j.apsusc.2014.03.006.

[24] Y. Yang, H. Wu, B. Liu, Z. Liu, Tumor microenvironment-responsive dynamic inorganic nanoassemblies for cancer imaging and treatment, Adv. Drug Delivery Rev. 179 (2021) 114004, https://doi.org/10.1016/j.addr.2021.114004.

[25] X.-Y. Huang, Z.-T. Chi, W. Yang, Y. Deng, W.-F. Xie, Synthesis of $Bi_2O_2CO_3/In(OH)_3 \cdot xH_2O$ nanocomposites for isopropanol sensor with excellent performances at low temperature, Sens. Actuators, B 361 (2022) 131715, https://doi.org/10.1016/j.snb.2022.131715.

[26] L.-Y. Zhu, K. Yuan, J.-G. Yang, H.-P. Ma, T. Wang, X.-M. Ji, J.-J. Feng, A. Devi, H.-L. Lu, Fabrication of heterostructured p-CuO/n-SnO_2 core-shell nanowires for enhanced sensitive and selective formaldehyde detection, Sens. Actuators, B 290 (2019) 233-241, https://doi.org/10.1016/j.snb.2019.03.092.

[27] V. Paolucci, M. Basso, V. Ricci, E. Colusso, M. Cattelan, E. Napolitani, A. Martucci, C. Cantalini, Pulsed-laser annealed amorphous/crystalline a-V_2O_5/VO_2

heterostructure for selective NO_2 and H_2 sensing, Sens. Actuators, B 428 (2025) 137235, https://doi.org/10.1016/j.snb.2025.137235.

[28] D. Zappa, V. Galstyan, N. Kaur, H.M.M. Munasinghe Arachchige, O. Sisman, E. Comini, "Metal oxide -based heterostructures for gas sensors"- A review, Analytica Chimica Acta 1039 (2018) 1-23, https://doi.org/10.1016/j.aca.2018.09.020.

[29] S. Yang, G. Lei, H. Xu, Z. Lan, Z. Wang, H. Gu, Metal Oxide Based Heterojunctions for Gas Sensors: A Review, Nanomaterials 11 (2021) 1026, https://doi.org/10.3390/nano11041026.

[30] V. Krivetskiy, I. Malkov, A. Garshev, N. Mordvinova, O.I. Lebedev, S. Dolenko, A. Efitorov, T. Grigoriev, M. Rumyantseva, A. Gaskov, Chemically modified nanocrystalline SnO_2-based materials for nitrogen-containing gases detection using gas sensor array, J. Alloys Compd. 691 (2017) 514-523, https://doi.org/10.1016/j.jallcom.2016.08.275.

[31] A. Hierlemann, R. Gutierrez-Osuna, Higher-Order Chemical Sensing, Chem. Rev. 108 (2008) 563-613, https://doi.org/10.1021/cr068116m.

[32] L. Mao, H. Jiang, Z. Dong, P. Huang, T. Gao, J. Pan, X. Xiao, Y. Du, X. Ren, Q. Hu, J. Xu, An artificial olfactory system with confined structures enhanced gas classification and potential esophageal cancer diagnosis, Sens. Actuators, B 447 (2026) 138775, https://doi.org/10.1016/j.snb.2025.138775.

[33] Pradyumn, P.B. Barman, A. Sil, S.K. Hazra, Recent advancement in selective gas sensors and role of machine learning, J. Alloys Compd. 1030 (2025) 180757, https://doi.org/10.1016/j.jallcom.2025.180757.

[34] Y. Jiang, L. Yao, Y. Hu, X. Liu, L. Xu, C. Zheng, L. Chen, J. Yang, X. Gao, An on-chip microarray platform for material-temperature optimization and gas discrimination, Sens. Actuators, B 409 (2024) 135633, https://doi.org/10.1016/j.snb.2024.135633.

[35] Z. Yang, Y. Liu, D. Chen, J. Miao, M. Chen, G. Liu, G. Gao, Y. Guo, D. Cui, Q. Li, A battery-free, wireless, flexible bandlike e-nose based on MEMS gas sensors for precisely volatile organic compounds detection, Nano Energy 127 (2024) 109711, https://doi.org/10.1016/j.nanoen.2024.109711.

[36] R. Thayil, S.R. Parne, Room Temperature n-Butanol Sensing with Bio-Functionalized Magnetic Nanoparticle-Integrated $MoSe_2$ Nanocomposites, Journal of Electronic Materials (2025), https://doi.org/10.1007/s11664-025-12508-z.

[37] R. Thayil, S.R. Parne, Morphology-tuned silver microrods decorated molybdenum disulfide nanocomposite for enhanced room temperature benzene sensing, Chemical Papers (2025), https://doi.org/10.1007/s11696-025-04482-x.

[38] G. Liu, E. Froudarakis, J.M. Patel, M.Y. Kochukov, B. Pekarek, P.J. Hunt, M. Patel, K. Ung, C.H. Fu, J. Jo, H.K. Lee, A.S. Tolias, B.R. Arenkiel, Target specific functions of EPL interneurons in olfactory circuits, Nat. Commun. 10 (2019) 3369, https://doi.org/10.1038/s41467-019-11354-y.

[39] L. Sun, R. Li, W. Zhan, Y. Yuan, X. Wang, X. Han, Y. Zhao, Double-shelled hollow rods assembled from nitrogen/sulfur-codoped carbon coated indium oxide nanoparticles as excellent photocatalysts, Nat. Commun. 10 (2019) 2270, https://doi.org/10.1038/s41467-019-10302-0.

[40] S. Park, M. Kim, Y. Lim, D. Oh, J. Ahn, C. Park, S. Woo, W. Jung, J. Kim, I.-D. Kim, Dual-Photosensitizer Synergy Empowers Ambient Light Photoactivation of Indium Oxide for High-Performance NO_2 Sensing, Adv. Mater. 36 (2024) 2313731, https://doi.org/10.1002/adma.202313731.

[41] M. Al-Hashem, S. Akbar, P. Morris, Role of Oxygen Vacancies in Nanostructured Metal-Oxide Gas Sensors: A Review, Sens. Actuators, B 301 (2019) 126845, https://doi.org/10.1016/j.snb.2019.126845.

[42] H. Huang, X. Li, J. Wang, F. Dong, P.K. Chu, T. Zhang, Y. Zhang, Anionic Group Self-Doping as a Promising Strategy: Band-Gap Engineering and Multi-Functional Applications of High-Performance CO_3^{2-}-Doped $Bi_2O_2CO_3$, ACS Catal. 5 (2015) 4094-4103, https://doi.org/10.1021/acscatal.5b00444.

[43] B. Yang, K. Lv, Q. Li, J. Fan, M. Li, Photosensitization of $Bi_2O_2CO_3$ nanoplates with amorphous Bi_2S_3 to improve the visible photoreactivity towards NO oxidation, Appl. Surf. Sci. 495 (2019) 143561, https://doi.org/10.1016/j.apsusc.2019.143561.

[44] Y. Cai, D. Chen, N. Li, Q. Xu, H. Li, J. He, J. Lu, A Self-Cleaning Heterostructured Membrane for Efficient Oil-in-Water Emulsion Separation with Stable Flux, Adv. Mater. 32 (2020) 2001265, https://doi.org/10.1002/adma.202001265.

[45] Z. Zheng, K. Liu, Y. Zhou, M. Debliquy, C. Zhang, Ultrasensitive room-temperature geranyl acetone detection based on Fe@WO_{3-x} nanoparticles in cooked rice flavor analysis, J. Adv. Ceram. 12 (2023) 1547-1561, https://doi.org/10.26599/JAC.2023.9220771.

[46] X. Li, B. Kang, F. Dong, Z. Zhang, X. Luo, L. Han, J. Huang, Z. Feng, Z. Chen, J. Xu, B. Peng, Z.L. Wang, Enhanced photocatalytic degradation and H_2/H_2O_2 production performance of S-pCN/$WO_{2.72}$ S-scheme heterojunction with appropriate surface oxygen vacancies, Nano Energy 81 (2021) 105671, https://doi.org/10.1016/j.nanoen.2020.105671.

[47] A. Dey, Semiconductor metal oxide gas sensors: A review, Materials Science and Engineering: B 229 (2018) 206-217, https://doi.org/10.1016/j.mseb.2017.12.036.

[48] N.A. Isaac, I. Pikaar, G. Biskos, Metal oxide semiconducting nanomaterials for air quality gas sensors: operating principles, performance, and synthesis techniques, Microchimica Acta 189 (2022) 196, https://doi.org/10.1007/s00604-022-05254-0.

[49] D. Meena, B. Singh, A. Anand, M. Singh, M.C. Bhatnagar, Phase dependent

selectivity shifting behavior of Cd_2SnO_4 nanoparticles based gas sensor towards volatile organic compounds (VOC) at low operating temperature, J. Alloys Compd. 820 (2020) 153117, https://doi.org/10.1016/j.jallcom.2019.153117.

[50] H. Gao, Y. Ma, P. Song, Z. Yang, Q. Wang, Three-dimensional reduced graphene oxide/cobaltosic oxide as a high-response sensor for triethylamine gas at room temperature, Materials Science in Semiconductor Processing 133 (2021) 105904, https://doi.org/10.1016/j.mssp.2021.105904.

[51] Y. Masuda, T. Itoh, W. Shin, K. Kato, SnO_2 Nanosheet/Nanoparticle Detector for the Sensing of 1-Nonanal Gas Produced by Lung Cancer, Sci Rep 5 (2015) 10122, https://doi.org/10.1038/srep10122.

[52] P.G. Choi, N. Shirahata, Y. Masuda, Tin oxide nanosheet thin film with bridge type structure for gas sensing, Thin Solid Films 698 (2020) 137845, https://doi.org/10.1016/j.tsf.2020.137845.